Engineering Structures 344 (2025) 121318

Contents lists available at ScienceDirect

Engineering Structures

journal homepage: www.elsevier.com/locate/engstruct

In-situ testing of the out-of-plane flexural behavior of hollow block masonry walls retrofitted with steel fiber reinforced mortar coating

Luca Facconi, Sara S. Lucchini, Fausto Minelli *, Giovanni Plizzari

Department of Civil, Architectural, Environmental Engineering and of Mathematics (DICATAM), University of Brescia, Italy

ARTICLE INFO

Keywords:
Masonry
Out-of-plane bending
Full-scale walls
In-situ testing
One-way spanning wall
Two-way spanning wall
Steel fiber reinforced mortar (SFRM)
Coating

ABSTRACT

The present work focuses on the discussion of the experimental results of three monotonic and quasi-static reverse cyclic tests performed to assess the out-of-plane behavior of hollow clay block masonry walls strengthened with coating. The latter consisted of a single 30 mm thick layer of mortar applied on the outer surface of masonry and reinforced with short (32 mm long) high strength steel fibers randomly spread within the mortar matrix. Compared to traditional laboratory tests, the ones conducted herein can replicate the actual boundary conditions occurring in actual structures as the test walls are part of a full-scale building tested in previous research. The test results provided insights into the stiffness, ductility, flexural and energy dissipation capacity of the walls. Additionally, considerations regarding equivalent viscous damping were also reported. Finally, using a classical arch thrust resisting model, an analytical evaluation of the out-of-plane flexural resistance of the unstrengthened walls was conducted to assess the potential out-of-plane strength improvement achieved through a coating of steel fiber reinforced mortar.

1. Introduction

Recent seismic events have emphasized the vulnerability of existing un-reinforced masonry (URM) buildings to out-of-plane (OP) failure mechanisms. These vulnerabilities are influenced by masonry typology, construction methods, and the era in which buildings were constructed. Depending on these factors, OP collapse can occur through various mechanisms, affecting both historic and modern structures.

In URM buildings, walls can have different structural functions related to the properties of the construction system [1]. In URM and confined masonry structures, walls act as load-bearing elements able to resist both static loads and seismic actions, including in-plane and OP forces, provided they are properly connected to the roof and floors. In masonry-infilled frames, the reinforced concrete (r.c.) frame is constructed first, and the masonry infill is typically considered a non-structural element, not intended to resist static or seismic loads. However, during seismic events, these infill walls inevitably interact with the frame, affecting both its in-plane and OP behavior.

The most frequent OP failure modes result from the lack of connections between bearing walls and horizontal elements as well as from the low axial stresses acting in the walls of the top stories. In addition, when in-plane and OP actions act together, the former can cause shear cracks having detrimental effect on the ability of the walls to resist OP bending. More in general, OP mechanisms are frequently the most critical mechanisms that considerably affect the seismic vulnerability of existing masonry buildings.

Several laboratory studies have been conducted to investigate OP bending, generally using specimens built in a laboratory setting. These studies provide valuable parametric insights [2–5] but often lack realism due to the difficulty in replicating actual wall-to-structure interactions, which are better captured through in-situ testing [6–8]. Calvi et al. [9] highlighted this limitation and, hence, underlined the importance of performing in-situ tests as the most viable and effective way to assess the real behavior of the member. Furthermore, according to FEMA 274 [10], the extraction of masonry subassemblies for laboratory testing may disturb the structural integrity, leading to reduced confidence in the test results due to the high scatter in the experimental data.

To improve the resistance of bearing walls against seismic OP actions, several retrofitting techniques have been developed, including fabric reinforced cementitious matrix (FRCM) systems [11–14], also known as textile reinforced mortar (TRM), and composite reinforced mortar (CRM) [15–17]. When connected to either one or both sides of

---

* Corresponding author.
E-mail addresses: luca.facconi@unibs.it (L. Facconi), sara.lucchini@unibs.it (S.S. Lucchini), fausto.minelli@unibs.it (F. Minelli), giovanni.plizzari@unibs.it (G. Plizzari).

https://doi.org/10.1016/j.engstruct.2025.121318
Received 2 April 2025; Received in revised form 15 August 2025; Accepted 8 September 2025

masonry walls, both FRCM and CRM proved to be very effective in improving the strength and ductility of members subjected to in-plane and OP cyclic actions. These methods offer advantages over traditional FRP strip-based solutions [18], which are usually more expensive and may suffer from debonding and degradation at elevated temperatures.

A relatively new technique, hereafter referred to as steel fiber reinforced mortar (SFRM), concerns the application of a 30–50 mm thick mortar layer reinforced with randomly distributed steel fibers. This system improves crack control, enhances durability, and offers greater resistance to corrosion compared to conventional r.c. coatings. This technique has been investigated by few studies that proved its effectiveness when applied to URM elements [19–22].

In previous experimental research [23], the authors tested a full-scale hollow block masonry building under reverse cyclic loading. The goal was to evaluate the effectiveness of SFRM coating in improving lateral strength after initial damage to the bare structure. The SFRM used was a cement-based mortar mixed with 60 kg/m^3 (0.76 % by volume) of double hooked-end steel fibers with a length of 32 mm and a diameter of 0.4 mm. Results showed that a single 30 mm-thick SFRM layer, applied only on the building's external surface, was sufficient to restore the building's structural integrity, increasing both maximum lateral capacity and deflection by over three times compared to the bare structure.

Based on these promising results, the present study investigates the potential utility of SFRM coating as a retrofitting method for improving the OP bending behavior of masonry walls. A test rig was designed to apply OP cyclic loading to the ground-floor walls forming the short sides of the test building mentioned above. Three specimens were tested under monotonic and cyclic conditions.

This paper presents and discusses the results of these OP tests, emphasizing the structural performances resulting from the use of single-sided strengthening with SFRM coating. Considerations about the observed failure mechanisms, the stiffness, the ductility and the ability of the wall to dissipate energy were reported and deeply analyzed. The tests focused on the OP behavior but did not account for the interaction between in-plane and OP mechanisms that typically occur in real cases involving bi-directional seismic loading conditions.

Since the tests conducted in this study do not provide information on the OP behavior of the un-strengthened (bare) walls, the final section of the manuscript aims to estimate the potential capacity improvement achieved through SFRM coating repair. To this end, the OP capacity of the bare walls was calculated using a simple arch resisting model generally used in the seismic assessment of existing buildings. Therefore, caution should be exercised regarding the reliability of these analytical results, as they have not been validated through tests on non-retrofitted walls.

2. Experimental program

2.1. Material properties

The properties of materials have been described in previous works [23,24] devoted to the study of the full-scale building including the walls tested herein. Thus, the mechanical properties of materials will be hereafter briefly summarized to provide the essential data about masonry and SFRM (Table 1).

The URM used in this research was made with 250 (length) x 190 (height) x 200 (width) mm^3 clay blocks with vertical holes (void area: 62 %) forming the running bond masonry pattern of the full-scale building. A ready-mix cement-based mortar (cement:hydraulic lime: sand – 1:2:9 by volume) filled the head and bed joints having an average thickness of about 10 mm. Clay blocks and mortar had a specific weight respectively of 6.0 kN/m^3 and 17.5 kN/m^3, leading to a specific weight of the composite masonry material equal to 7.45 kN/m^3. The main mechanical properties of masonry and its components are summarized in Table 1.

Table 1
Mean properties of materials.

Property	Code reference	Number of samples	Mean	CoV
			[MPa]	[%]
Masonry				
Mean compressive strength of mortar (f_{cm})	EN 1015–11 [25]	60	8.9	10.3
Mean compressive strength of units (f_b) parallel to holes	EN 772–1 [29]	16	12.7	13.5
Compressive strength parallel to holes (f_{mv})	EN 1052–1 [30]	3	2.93	28.8
Compressive strength perpendicular to holes (f_{mo})	EN 1052–1 [30]	3	0.59	22.1
In-plane diagonal shear strength (τ_0)	ASTM E519–02 [31]	3	0.26	24.0
Elastic modulus parallel to holes (E_m)	EN 1052–1 [30]	3	8980	26.3
SFRM				
Compressive cube strength (f_c)	EN 1015–11 [25]	84	35.1	15.6
Modulus of rupture	EN 1015–11 [25]	42	8.8	19.2
Secant elastic modulus (E_c)	EN12390–13 [26]	3	20,430	8.4
Limit of proportionality $f_{L,m}$	EN 14651 [27]	13	3.5	18.4
Flexural strength $f_{R,1m}$ (CMOD=0.5 mm)	EN 14651 [27]	13	5.4	21.7
Flexural strength $f_{R,2m}$ (CMOD=1.5 mm)	EN 14651 [27]	13	6.0	17.3
Flexural strength $f_{R,3m}$ (CMOD=2.5 mm)	EN 14651 [27]	13	6.0	18.0
Flexural strength $f_{R,4m}$ (CMOD=3.5 mm)	EN 14651 [27]	13	5.4	24.5

The SFRM, with a specific weight of 21.4 kN/m^3, consisted of a ready-mix cement-based mortar containing 60 kg/m^3 of double hooked-end steel fibers having a length of 32 mm, a fiber diameter of 0.4 mm and a tensile strength higher than 2100 MPa. The compressive and flexural strengths of the material were determined by testing 40 x 40 x 160 mm^3 prisms according to EN 1015–11 [25]. In order to determine the elastic secant modulus, uniaxial compression tests were performed in compliance with EN 12390–13 [26] on three cylindrical specimens measuring 210 mm in length and 80 mm in diameter. To characterize the tensile behavior of SFRM, three-point bending tests on notched beams with dimensions of 150 (depth) x 600 (length) x 40 (thickness) mm^3. The test setup followed the procedure outlined in EN 14651 [27], except for the beam thickness, which was reduced from the standard 150 mm to 40 mm to better reproduce the bidimensional orientation of fibers within the coating layer. As required by the Eurocode 2 – Annex L [28], the tests allowed determining the limit of proportionality $f_{L,m}$ as well as the residual flexural strengths $f_{R,1m}$, $f_{R,2m}$, $f_{R,3m}$ and $f_{R,4m}$ corresponding respectively to CMODs of 0.5 mm, 1.5 mm, 2.5 mm and 3.5 mm. The mean values of the mechanical properties resulting from the tests described above are reported in Table 1. The SFRM classification, according to Eurocode 2, is 5c, considering mean values. Using these parameters, the mean ultimate uniaxial tensile strength of the SFRM ($f_{Ft3,ef}$) can be estimated by the equation provided in clause L5.5.2 of the Eurocode 2:

$$f_{Ft3,ef} = 0.57 \cdot f_{R,3m} - 0.26 \cdot f_{R,1m} = 2.02\text{MPa} \tag{1}$$

By assuming an average coating thickness of 30 mm, which matches that adopted in this study, the corresponding mean ultimate tensile resistance is approximately 61 kN/m. This value falls within the typical tensile resistance range of 40–100 kN/m, commonly exhibited by commercially available GFRP, CFRP, and basalt fiber-reinforced meshes or grids.

2.2. Specimen properties and test set-up

Even though it was constructed for experimental purposes, the building presented all the typical characteristic elements of a real two-story house. These included a r.c. strip foundation supporting the bearing walls, r.c. chords laid on the top side of the walls, one-way floors provided with a r.c. topping slab and a wooden roof. The good interlocking of the clay blocks placed at the wall corners ensured the effective connection between orthogonal walls that allowed to prevent potential overturning mechanisms of the facades. Thus, from the structural point of view, the main difference with respect to a typical residential building was represented by the lack of plaster on both sides of the bearing walls and by the presence of robust connection between floors and walls. This latter feature is not always present in existing buildings that were not originally designed to withstand seismic forces. Moreover, the experimental prototype cannot account for the material degradation caused by aging and exposure to environmental conditions.

The OP tests were carried out after testing the whole building under lateral loading [23]. The test program included three walls loaded by either line or point loads, in place of the uniformly distributed load configurations sometimes used by researchers to better approximate the actual distribution (i.e., proportional to mass distribution) of seismic loads. In fact, the use of devices such as air-bags [32,33] is a good option to obtain a uniform distribution of the lateral load acting on the wall surface. However, when performing reversed-cyclic bending tests, particular care must be paid to properly control the air-bag system, especially during the deflating phase. Furthermore, since the airbag [34, 35] is placed on both sides of the wall to perform loading reversal, the visual inspection of the damage evolution is generally difficult to carry out. For these reasons, in this research the use of line and point loads was preferred to air-bags, conscious of the possible influence that such loading configurations may potentially have on the development of the crack pattern. Indeed, even when properly distributed stiff plates over the wall surface, point and line loads tend to induce localized disturbed regions that can affect the failure mechanisms, potentially leading to an underestimation of the actual capacity.

As two different boundary conditions were considered, the specimens were grouped into two typologies (Table 2): the former, hereafter referred to as “one-way spanning wall”, included the two strip walls (i.e., WO1 and WO2) subjected to simply supported boundary conditions; the latter, named as “two-way spanning wall”, referred to the wall (i.e. WO3) supported along four sides. All the walls were externally strengthened with SFRM layer, having an average thickness of 30 mm ± 2 mm. A detailed description of the specimen preparation, details and testing procedure is reported in the following sub-sections.

2.2.1. One-way spanning wall

The two one-way spanning walls had a total height of 2520 mm and a width of 1000 mm (Fig. 1a). To obtain these dimensions, a concrete circular saw was used to perform four 230 mm deep vertical cuts through the entire height of the ground story walls of the North façade of the buildings (Fig. 1b). To maintain the alignment of cutting, a vertical sliding guide was mounted close to the inner surface of the wall (Fig. 2). To minimize the potential damage to clay blocks, the saw was positioned to intersect the maximum number of head joints.

The top and the bottom edge were respectively restrained by the concrete chord located along the perimeter of the floor and by the concrete foundation of the building. A single 8 mm diameter steel rebar, with a mean yield strength of 500 MPa, connected the SFRM coating to the foundation. During the coating application process, the rebar was grouted to the foundation using epoxy [23]. As shown in Fig. 1a, the rebar was located 240 mm from the left side of the panel.

Fig. 3 shows the schematic of the test set-up adopted to perform the four-point bending tests. The test-rig consists of a steel reaction frame placed inside the building and connected to the strong floor forming the foundation of the structure.

A 200 kN capacity electromechanical screw jack, connected to the frame, was used to apply the horizontal load, which was transferred from the jack to the distributor steel beam by a hinged connection provided with a tension-compression load cell. The distributor beam divided the total lateral load equally into two-point loads, which were converted into line loads using horizontal loading steel beams. These beams had approximately the same width as the wall and a total contact area of 900 × 140 mm^2 at the beam-to-wall interface (Fig. 3). To allow load reversal, the loading beams were positioned on both sides of the wall and clamped together using Dywidag bars that passed through the wall. The horizontal beams were placed in direct contact with the wall surface, without any intermediate material at the beam-to-wall interface. The electromechanical jack allowed the application of the lateral load at a constant rate of about 0.025 mm/s. Based on an accurate evaluation of the self-weight of materials forming the floors and the walls of the building, the total axial load acting at the top of the two specimens resulted equal to 20.8 kN.

Fig. 3 also reports the details of the instrumentation used to continuously monitor the specimens. The OP deflections were measured by three horizontal potentiometers (i.e., HM1 to HM3) placed on the inner uncoated side of the wall and five horizontal potentiometers (i.e., HC1 to HC5) located at different heights over the SFRM coating. An additional potentiometer (HC6) was placed at the same location as the concrete chord running over the top of the wall to keep the lateral deflection of the whole building under control. A series of vertical potentiometers (i.e., V1 to V4) were used to detect the flexural cracks expected to form on the outer surface of the SFRM coating.

The walls were tested under displacement control by gradually increasing the horizontal net deflection (δ), which was measured by potentiometer HC3. This deflection was calculated by subtracting half the average of the displacements recorded by instruments HC1 and HC5 from the displacement recorded by HC3. Note that all the results presented below assume that the deflection and the corresponding load are positive when the wall is pushed outward and negative when it is pulled inward.

A different loading procedure was adopted for testing the two specimens. In fact, the deflection of wall WO1 was monotonically increased up to a maximum value of about + 7.5 mm and then, after complete unloading, it was monotonically re-loaded up to a deflection of − 11 mm. On the contrary, wall WO2 was subjected to cycles of increasing amplitude according to the loading history depicted in Fig. 4a. Because of the adopted single-sided retrofitting, the displacement capacity of the walls in the positive direction (outward) was lower than that observed in the negative direction. This phenomenon was

Table 2
Summary of the testing program.

Specimen	Support condition	Wall dimensions			SFRM coating		Type of test
ID		height	width	t_m	# of layers	t_{coat}	
		[mm]	[mm]	[mm]	[-]	[mm]	
WO1	One-way	2520	1000	200	1	30	Monotonic
WO2	One-way	2520	1000	200	1	30	Reverse-cyclic
WO3	Two-way	2520	4250	200	1	30	Reverse-cyclic

Note: t_m = thickness of masonry walls; t_{coat} = average thickness of SFRM coating

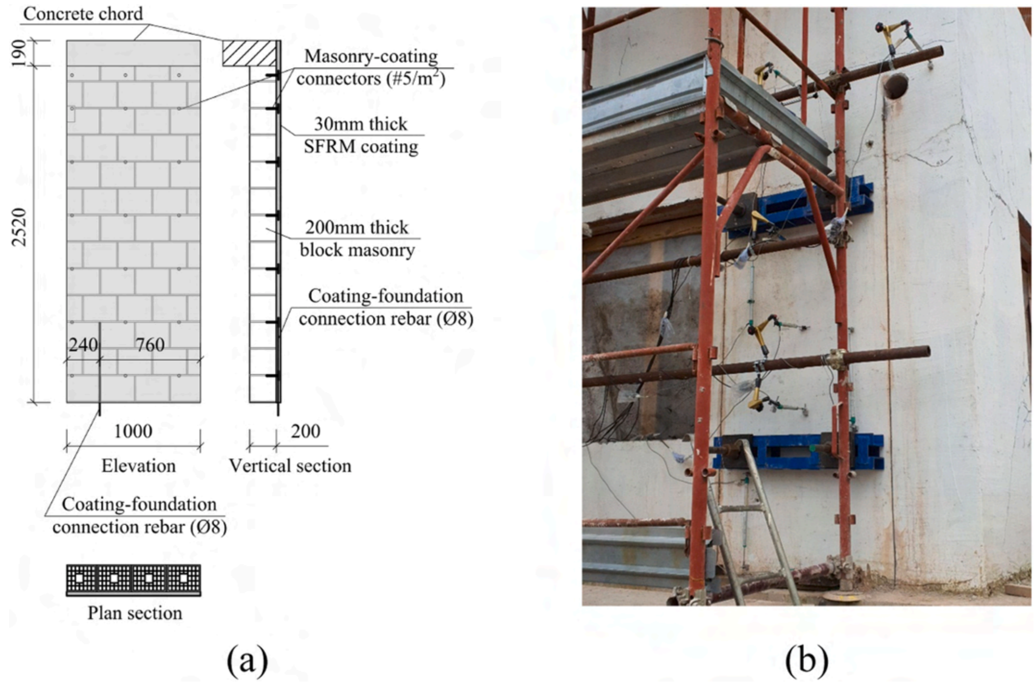

Fig. 1. Geometry of the one-way spanning walls: (a) schematic and (b) outside view of the specimen WO2.

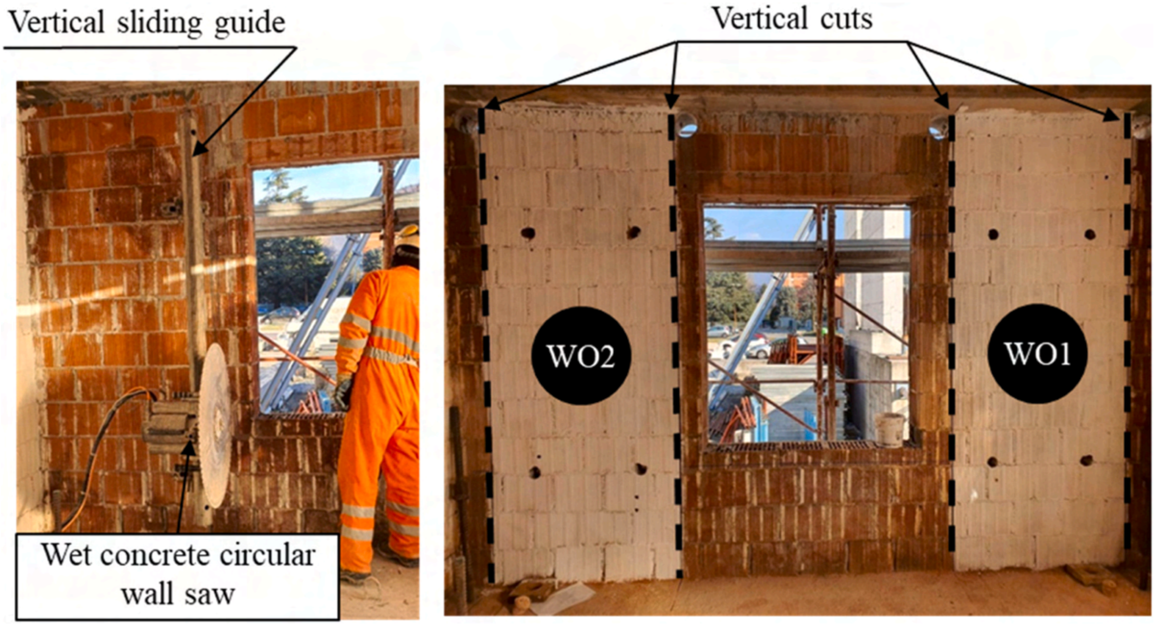

Fig. 2. Preparation of the one-way spanning walls (inside view).

related to the early crushing of hollow clay blocks located at the top end of the wall. Therefore, when the post-peak load dropped to approximately 85 % of the wall's maximum capacity in the positive direction, the loading protocol was adjusted. In the subsequent loading cycles, the lateral deflection was increased only in the negative direction, while the positive maximum deflection was no further increased.

2.2.2. *Two-way spanning wall*

Fig. 5 shows the geometry of the two-way spanning wall WO3, forming the south façade of the test building. The top and the bottom edge of the wall were restrained by the concrete chord and the foundation of the building, respectively. The SFRM coating was anchored to the foundation using nine 8 mm diameter rebars, spaced at 500 mm, with a mean yield strength of 500 MPa.

The test set-up, illustrated in Fig. 6, is similar to that used for testing the one-way spanning wall. A 500 kN capacity screw jack was fixed to a steel frame positioned on the ground floor and anchored to the building foundation. The jack was connected to the loading system via a steel hinged assembly equipped with a tension-compression load cell. A vertical steel beam at the end of the hinge split the lateral load into two equal forces, which were further divided into two-point loads by horizontal loading beams positioned respectively at 630 mm and 1890 mm above the foundation. Each point load was applied through 400 × 400 mm^2 steel plates placed on the inner side of the wall. On the

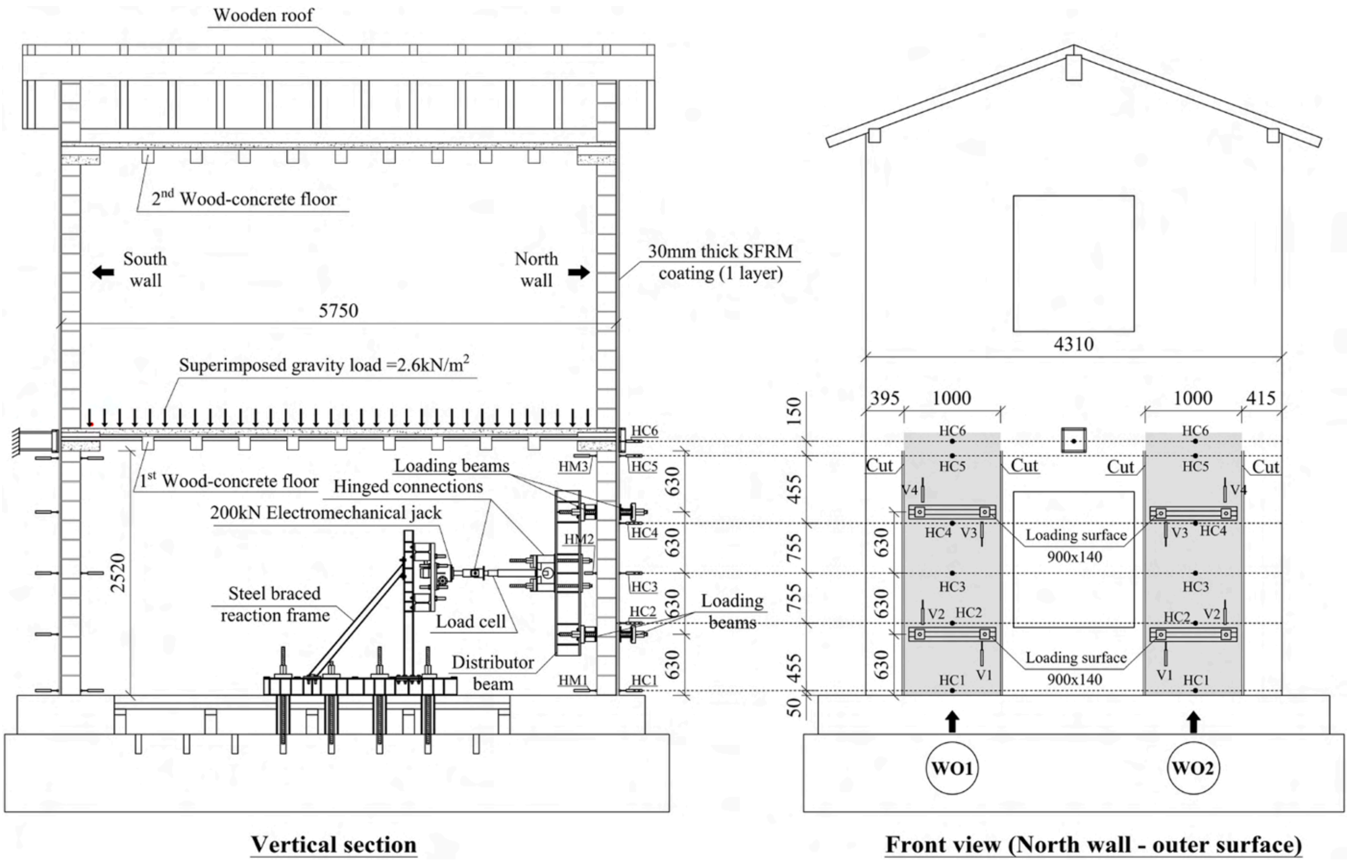

Fig. 3. Test set-up adopted for the one-way spanning walls (dimensions in [mm]).

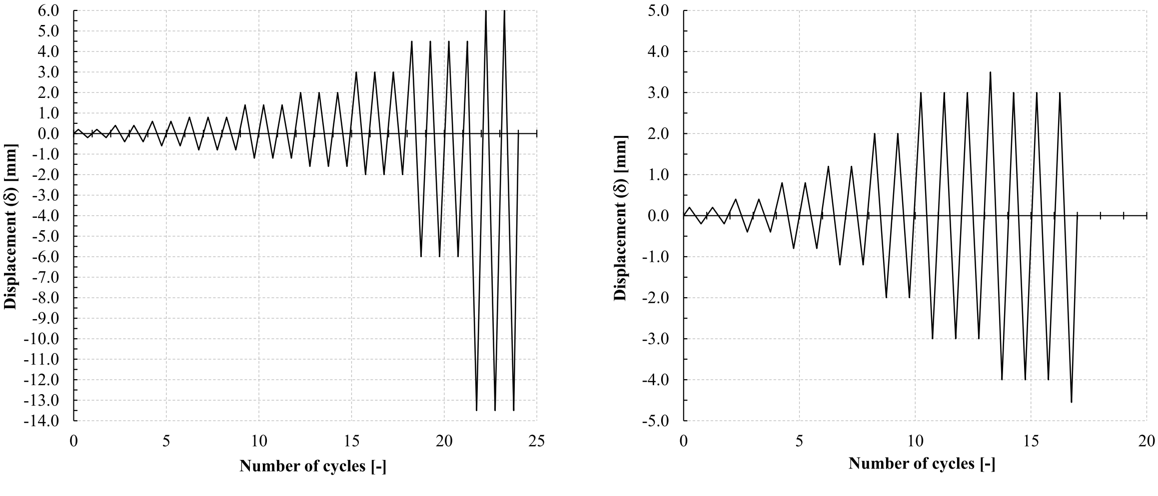

(a)

(b)

Fig. 4. Loading history: (a) one-way spanning wall (WO2); (b) two-way spanning wall (WO3).

outer side, four 400 × 400 mm^2 steel plates were placed on the SFRM coating surface and clamped to the corresponding inner plates using Dywidag bars, allowing loading reversal.

To measure the wall's OP response, 11 potentiometers were installed outside the building. Devices HW1 to HW3, HC1 to HC5, and HE1 to HE3 measured horizontal deflections over the SFRM coating, while HM1 to HM3, placed at the same height as HC1, HC3, and HC5, recorded horizontal deflections on the wall's uncoated surface. Additional sensors V1, V2, H1, and H2 detected vertical and horizontal crack formation.

Reverse cyclic testing was carried out under displacement control at a constant rate of 0.025 mm/s. The target displacements, as shown in Fig. 4b, correspond to the horizontal net deflection (δ) measured by instrument HC3. Positive and negative values indicate outward and inward deflections, respectively.

3. Test results

The present section reports a detailed discussion of the experimental

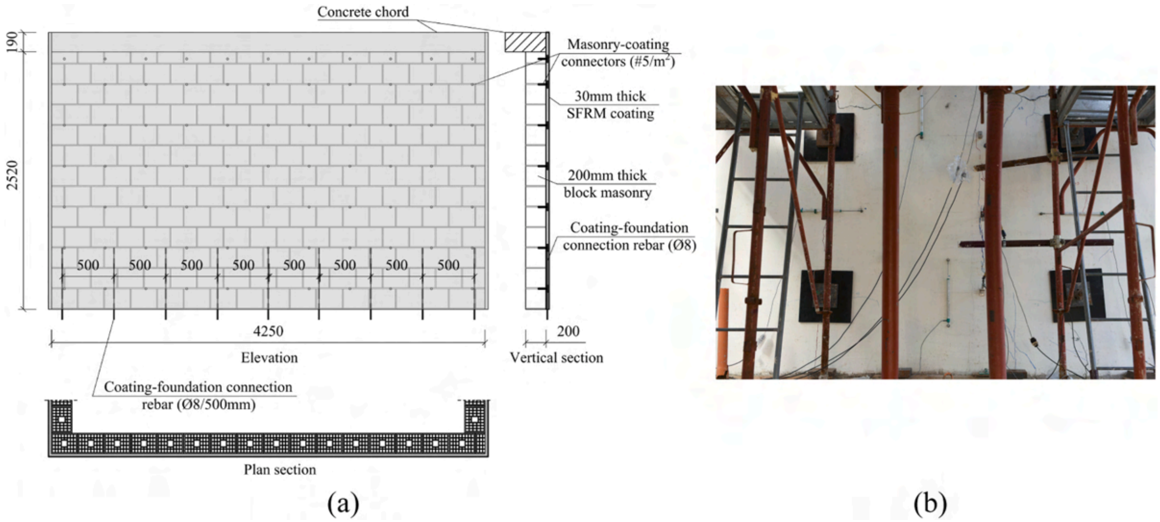

Fig. 5. Geometry of the two-way spanning wall: (a) schematic and (b) outside view.

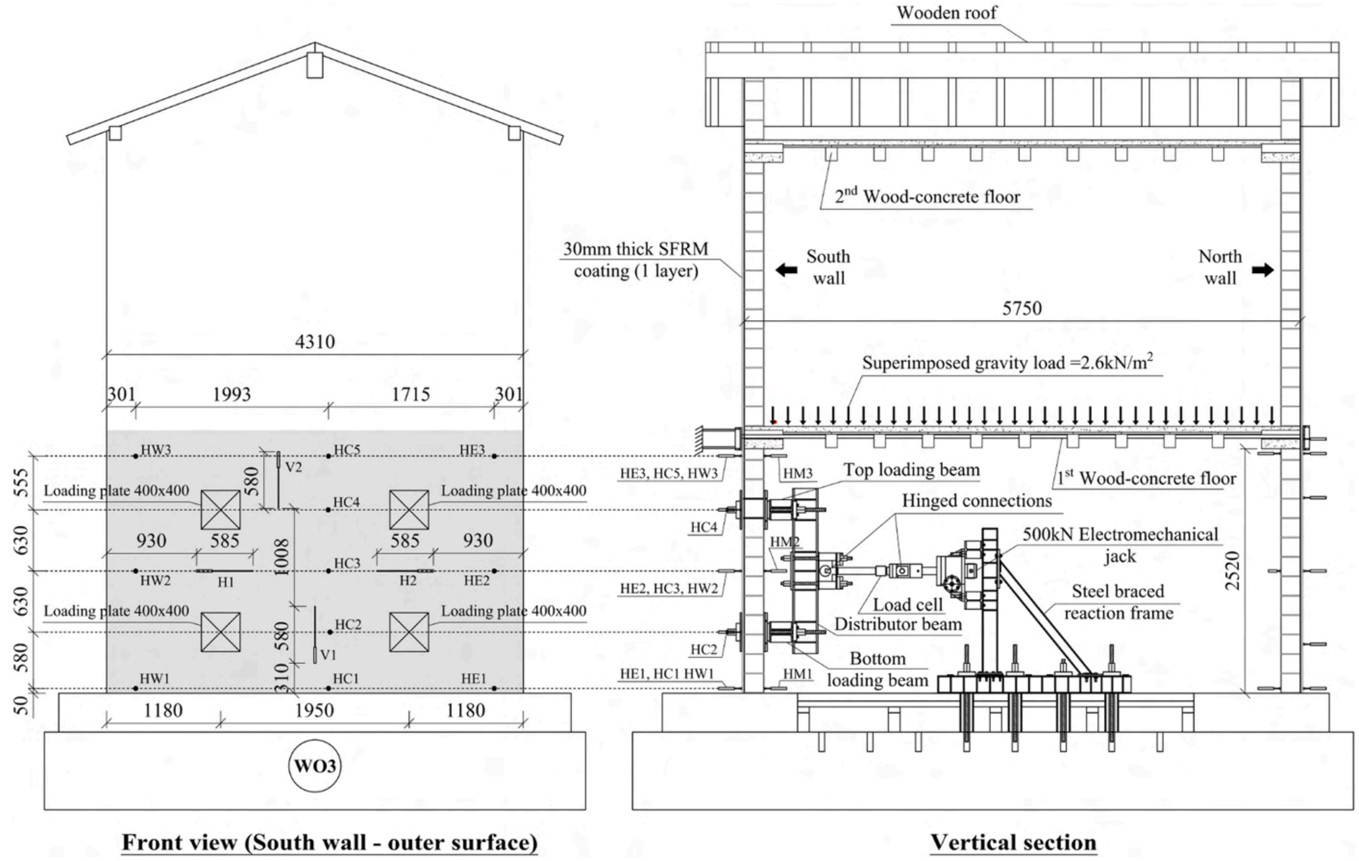

Fig. 6. Test set-up adopted for the two-way spanning wall (dimensions in [mm]).

results provided by the tests performed on the three specimens. Two subsections have been included to separately describe the response of the "one-way spanning walls" and of the "two-way spanning wall".

3.1. One-way spanning walls

3.1.1. Load-deflection response and damage evolution

The total lateral load (V) applied to the wall was plotted against the net lateral deflection (δ) detected at mid-height (Fig. 7). Fig. 7a shows the curve resulting from the monotonic test conducted on wall WO1. To better understand the wall's behavior, it is worth considering also the crack patterns illustrated in Fig. 8. Prior to the test, the wall exhibited pre-existing cracks from earlier cyclic loading conducted on the full-scale building [23]. In particular, a horizontal crack at the wall base was due to global rocking of the building during previous lateral loading, while two horizontal cracks near the upper loading beams resulted from the building's torsional response. At the time of OP testing, the base crack had closed completely, but the upper cracks on the outer surface remained partially open, with a residual width of about 0.1 mm. These were monitored by the potentiometer V4 on the

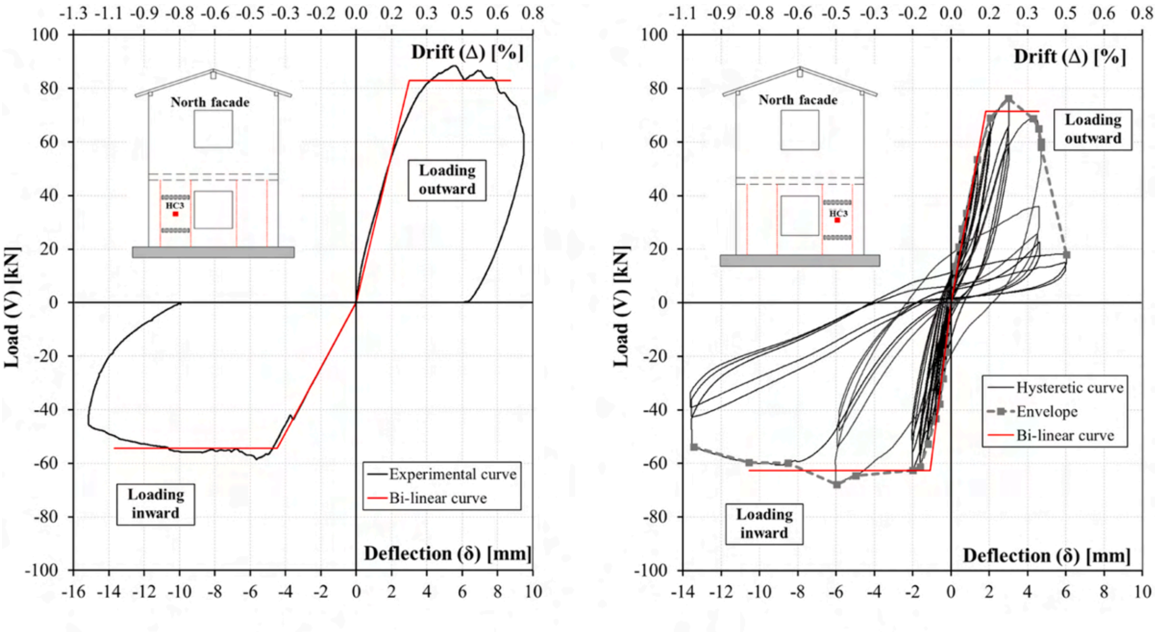

(a) (b)

Fig. 7. Load-deflection response of the one-way spanning walls: (a) wall WO1; (b) wall WO2.

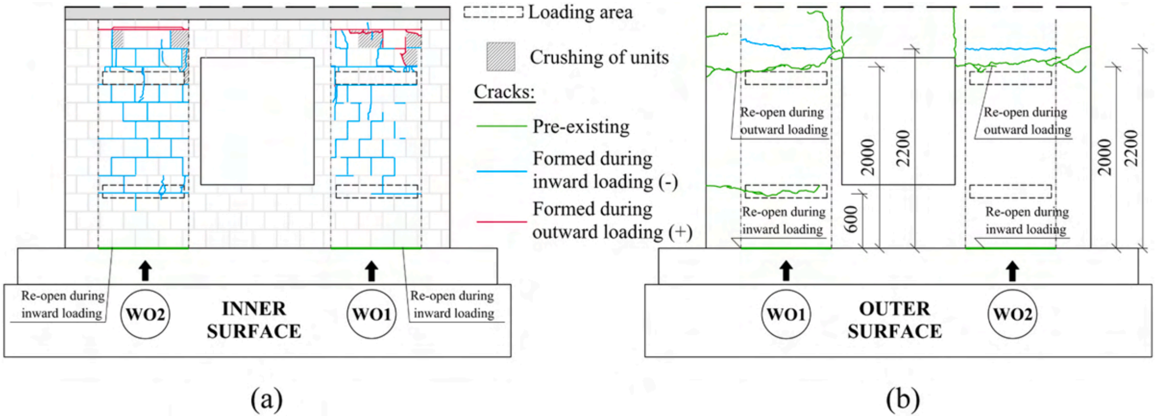

Fig. 8. Ultimate crack patterns detected on both the (a) inner and the (b) outer surface of the wall WO1 and WO2 (dimensions in [mm]).

SFRM-coated surface (Fig. 3).

The load-deflection curve of Fig. 7a presented an initial linear trend, with a slight stiffness reduction at a deflection of approximately 0.3 mm and a corresponding load of 14 kN. The first visible flexural crack formed along a horizontal joint near the top of the wall's inner surface (red crack in Fig. 8a). The pre-existing crack above the upper loading beam on the outer face (green crack in Fig. 8b) also began to widen once the load exceeded + 14 kN. By further increasing the load, no other significant cracks appeared on the specimen. However, the base crack inside the building reopened. The lateral load increased to + 88.5 kN, with a corresponding deflection of + 5.6 mm. At this stage, the red and green cracks reached widths of 0.9 mm and 1.3 mm, respectively. In the post-peak stage, the capacity gradually decreased, with a 15 % reduction recorded at a deflection of + 8.8 mm. Loading continued to a deflection of + 9.5 mm and load of + 63 kN, after which the wall was unloaded, leaving a residual deflection of + 6.5 mm.

The test was then resumed by re-loading the specimen inward. The negative branch of the curve shown in Fig. 7a, which originally started at the end of the unloading curve reported in the first quadrant of the graph, was shifted so that the residual deflection of + 6.5 mm appeared as the new zero. The load increased linearly to a maximum of − 58.4 kN at a deflection of − 5.6 mm. The base crack on the outer surface continued to widen, and a new crack (light-blue in Fig. 8b) initiated at a load of about − 20 kN, eventually reaching 0.2 mm in width. Multiple new horizontal cracks also appeared on the inner side (light blue in Fig. 8a), especially near the mid-height horizontal and vertical masonry joints. As the inward displacement increased, the blue crack (Fig. 8b) on the SFRM coating widened to 1 mm at the ultimate deflection of − 15 mm. The corresponding load had dropped to 22 % below peak capacity. At the end of the test, localized crushing was observed in the masonry units at the top of the wall's inner surface.

Fig. 9 illustrates the progression of the vertical deflection shape of wall WO1. When loading the wall outward, the deflected shape remained almost symmetric up to a midspan deflection of + 2/ + 2.5 mm. As deflection increased, the displacement measured at the top (by sensor HC4) grew significantly as compared to that detected at the bottom (by sensor HC2), indicating the formation of a plastic hinge near the upper loading point. This was confirmed by widening of the upper horizontal crack. Additionally, sensor HC6 detected a residual displacement due to severe damage in the first masonry course. The

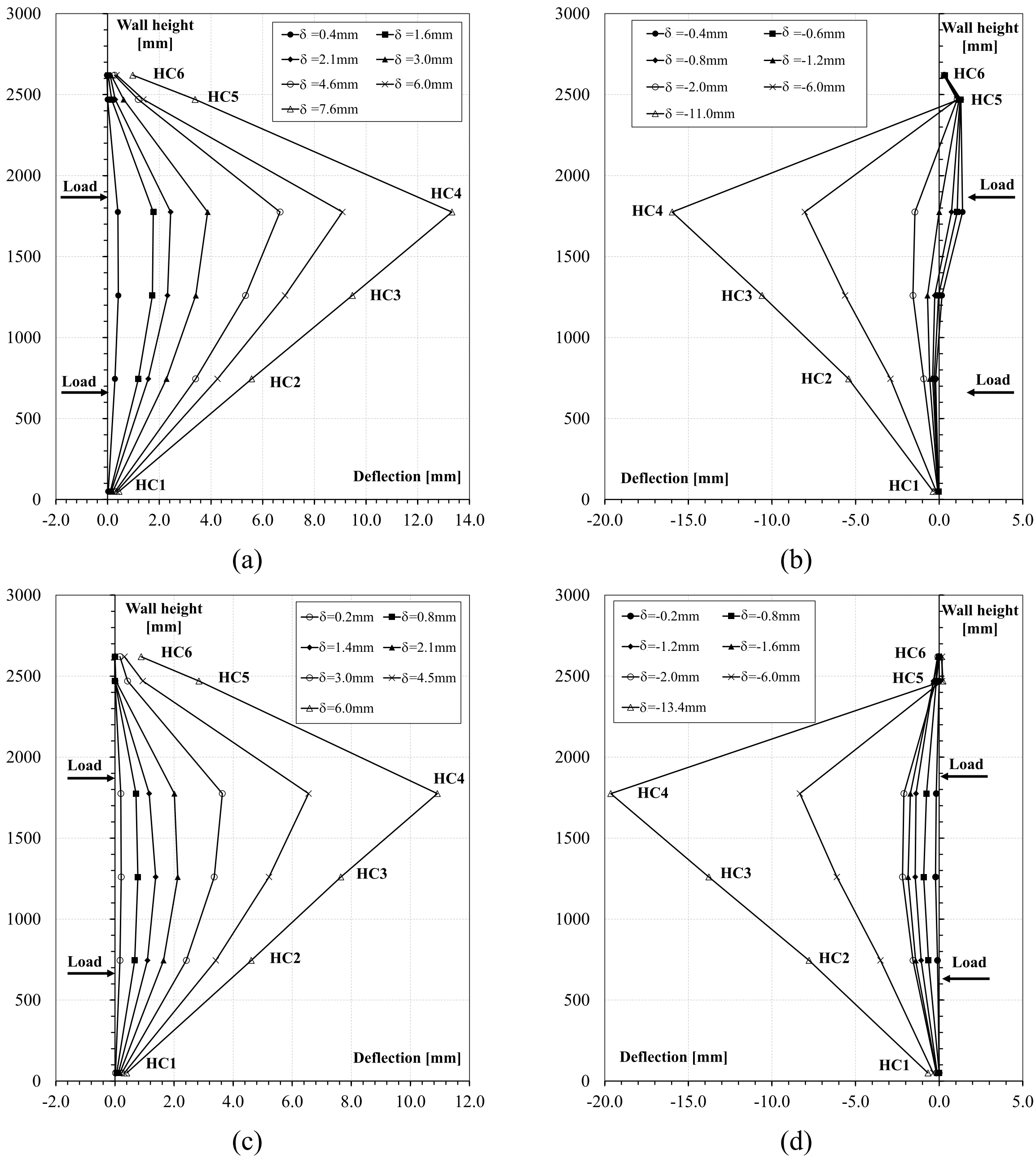

(a) (b) (c) (d)

Fig. 9. Vertical deflected profile at different mid-span deflection (δ): wall WO1 (a) positive and (b) negative loading direction; wall WO2 (c) positive and (d) negative loading direction.

curves in Fig. 9b show that damage concentration occurred in the top region during negative loading. The deflections detected by HC4 (Fig. 6) prove that a plastic hinge formed at approximately 2.2 m from the wall base, which corresponds to roughly 85 % of the wall height.

A summary of the main test results is reported in Table 3, including the maximum lateral resistance (V_{max}) and the corresponding deflection

Table 3
Summary of main test results.

Specimen	1)	V_{max} [kN]	δ_{max} [mm]	V_u [kN]	δ_u [mm]	Δ_u [%]	K_i [KN/mm]	V_y [kN]	δ_y [mm]	δ^*_u [mm]]	Δ^*_u [%]	μ [-]
WO1	+	88.5	5.6	74.8	8.8	0.70	27.6	83.0	3.0	8.8	0.70	2.9
	- 2)	58.4	5.6	45.6	15.0	1.19	12.2	54.4	4.5	13.7	1.09	3.0
WO2	+	76.2	3.0	18.0	6.0	0.48	39.4	71.5	1.8	4.6	0.37	3.3
	-	69.9	6.0	53.9	13.4	1.06	57.8	62.7	1.1	10.5	0.83	12.1
WO3	+	215.0	3.0	139.0	3.9	0.31	130	206	1.6	3.0	0.24	1.9
	-	215.0	3.0	190.1	4.8	0.38	107	199	1.7	4.8	0.38	2.8

Note: 1) (+) Outward loading; (-) Inward loading
2) The actual origin of the curve is not zero but the residual deflection at unloading (δ=+6.5 mm).

(δ_{max}), the ultimate resistance (V_u) and the related ultimate deflection (δ_u) and drift (Δ_u).

Fig. 7b presents the hysteretic response of wall WO2 along with its envelope curve, whose construction methodology has been reported in the next sub-section. The wall exhibited a behavior comparable to that of wall WO1. Following an initial linear response, a first reduction in stiffness was observed at a mid-span deflection of about + 0.2 mm, corresponding to a load of + 13.6 kN. This change in slope, evident in the envelope curve, was associated with the initiation of a horizontal crack (red) near the top of the wall, as shown in Fig. 8a. As loading continued, the pre-existing horizontal crack (green) near the upper loading beam (Fig. 8b) began to reopen once the applied force reached + 26 kN at a deflection of + 0.55 mm. This crack progressively widened, reaching 0.4 mm at the peak load of + 76.2 kN and a deflection of + 3.0 mm. With further displacement, the crack width rapidly increased to 0.9 mm when the deflection reached + 4.3 mm and the load dropped to + 68 kN, corresponding approximately to 89 % of the peak capacity. Beyond this point, a sharp reduction in resistance was observed. The ultimate load in the positive direction was + 18.0 kN, recorded at a lateral deflection of + 6.0 mm.

Under negative loading, a single horizontal crack (blue) formed on the coating surface (Fig. 8b), together with multiple cracks crossing mortar joints at mid-height (Fig. 8a). Repeated cycles resulted in clearly visible damage to the masonry units near the top of the wall, causing a sudden stiffness drop at a deflection of − 2.0 mm. The horizontal blue crack widened significantly, from an initial width of 0.05 mm to 0.8 mm when the deflection reached − 6.0 mm. The load then reduced gradually, reaching a residual strength of − 53.9 kN at a deflection of − 13.4 mm.

The deflected shape diagrams in Fig. 9c and d highlight the concentration of damage near the upper loading point. Similar to the monotonic test, the deflected shape evolved from symmetric to asymmetric as damage accumulated. Both walls showed increasing residual displacements at their top and bottom sections, likely due to masonry crushing, SFRM cracking, and horizontal sliding. These support degradations may influence the full activation of OP bending mechanisms. Further investigation performed by using advanced tools like 2D digital image correlation and R-CNN techniques [36] is recommended to better capture crack development and damage progression.

3.1.2. *Initial stiffness, ultimate drift and ductility*

In order to better compare the initial stiffness and the ductility, the experimental envelope curves were bi-linearized by the approach recommended by the Italian building code (NTC18) [37], which is described by the schematic of Fig. 10. The envelopes curves were obtained by connecting the peak load points recorded during the first loading cycle at each level of imposed lateral displacement. For the specimen WO1, the whole monotonic curve without the unloading branches was considered. The curves resulting from bi-linearization are defined by five parameters, namely the initial stiffness K_i, which is conventionally assumed as 0.6 $V_{max}/\delta_{0.6}$, the deflection ($\delta_{0.6}$) at 60 % of the maximum resistance (V_{max}) on the pre-peak curve, the deflection at the elastic limit (δ_y), the yield resistance (V_y) and the ultimate deflection ($\delta^*_u \leq \delta_u$) corresponding to a conventional ultimate resistance not lower than 0.85 V_{max}. The value of V_y can be found by equating the areas subtended by the experimental bi-linear curve up to the deflection δ^*_u. Table 3 reports the parameters of the idealized curves plotted in Fig. 7.

In order to quantify the ability of the wall to undergo large OP deflections without losing bearing capacity, a displacement ductility index was calculated as follows:

$$\mu = \frac{\delta_u^*}{\delta_y} \tag{2}$$

Finally, the ultimate drifts related to both the actual and the idealized curves were calculated respectively as $\Delta = 2\delta/h$ and $\Delta^* = 2\delta^*/h$, assuming the effective height h= 2520 mm.

According to the experimental results, the two walls had initial stiffnesses ranging from 12.2 kN/mm to 57.8 kN/mm. As expected, the lowest value of 12.2 kN/mm was extrapolated from the response of WO1 under negative loading, which was significantly affected by the damage cumulated during the positive loading phase. Regarding positive loading, the initial stiffness exhibited by wall specimen WO2 was approximately 1.4 times that of WO1.

Both walls exhibited a similar ductility of $\mu \approx 3$ in the positive direction. Considering the wall WO2, the ductility exhibited in the negative direction (μ=12.1) was about 3.6 times the one observed in the positive direction. This significant increase of ductility could be explained by considering the contribution of the reinforcing bar at the base of the wall, which contributes to the bending capacity of the base section during inward loading phase. On the contrary, when loading the wall outward, the tension side cannot exploit the tensile contribution of the reinforcement and, therefore, the ductility is mainly governed by progressive crushing of masonry and SFRM located on the compressive side of the member.

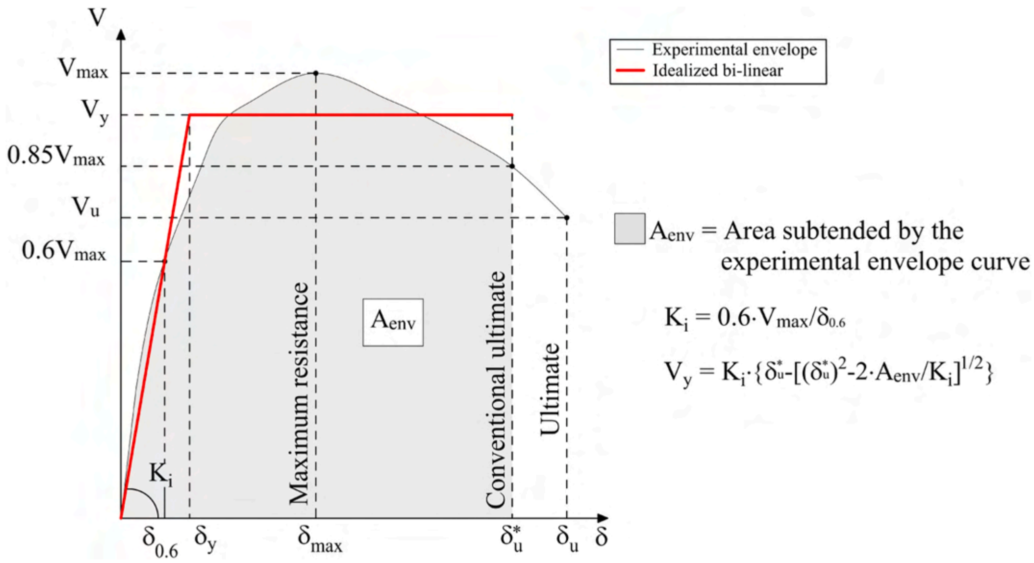

Fig. 10. Idealized load (V)-deflection (δ) bi-linear curve [37].

3.1.3. Energy dissipation and equivalent viscous damping

The dissipated energy (E) is presented in terms of cumulative energy dissipation, defined as the sum of energy dissipated over successive loading cycles. In Fig. 11a, the dissipated energy is plotted against the maximum negative deflection, which corresponds to the negative displacement (δ^{-}_{max}) at the negative peak load (V^{-}_{max}) attained within each loading cycle. Regarding the specimen WO2, the energy dissipation increased slowly until the up to a deflection of about 2 mm. For higher deflections the damage became more pronounced leading to a considerable increase in the area enclosed within each cycle, particularly in the negative loading direction. For deflections ranging from 2 mm to 13.5 mm, the cumulated energy increased from about 0.45 kJ to a maximum of 2 kJ, corresponding to an increase of 344 %.

Energy dissipated can be also represented by the so called equivalent hysteretic viscous damping ratio (ξ_{eq}), which is here computed according to the following formulation adapted from [38]:

$$\xi_{eq} = \frac{1}{2\pi}\frac{E_{d,i}}{E_{s,i}} = \frac{1}{\pi}\frac{E_{d,i}}{\left(V^{+}_{\delta 0,i}\cdot\delta^{+}_{0,i} + V^{-}_{\delta 0,i}\cdot\delta^{-}_{0,i}\right)} \tag{3}$$

where $E_{d,i}$ is the energy dissipated within each loading cycle whereas $E_{s,i}$ represents the elastic strain energy. The approach adopted to calculate the input strain energy is based on the evaluation of the lateral forces ($V^{+}_{\delta 0,i}$; $V^{-}_{\delta 0,i}$) corresponding to the maximum deflections ($\delta^{+}_{0,i}$; $\delta^{-}_{0,i}$) that characterized each loading cycle both in positive and negative direction (Fig. 11b). The evolution of the viscous damping ratio against maximum negative deflection δ^{-}_{max} is shown in Fig. 11b. For each test wall, the diagram presents three curves representing the damping ratios calculated for the 1st, 2nd, and 3rd cycles performed at the same drift level. Considering the wall WO2, a gradual reduction of ξ_{eq} from 16 % to about 6–8 % was observed during the early stages of the test, when cracked areas were still limited. As the damage level increased after attaining $\delta^{-} = 2$ mm, the damping ratio tended to increase up to maximum values of about 18 % because of the sharp increase of energy dissipation observed especially during the negative loading stages.

The literature lacks OP cyclic tests conducted on masonry walls strengthened with SFRM coatings. As a result, no reference values for equivalent viscous damping are currently available to validate the results discussed herein. Gattesco et al. [17] and Gams et al. [39] reported values and trends of the damping ratios similar to those shown in Fig. 11b, but their experiments referred to elements strengthened with single-sided CRM subjected to in-plane loading. Some relevant data referring to OP tests can be found in studies investigating one-way spanning elements strengthened on one or both sides using FRCM/TRM systems. Ismail and Ingham [40] conducted flexural tests on slender, double-wythe solid brick walls strengthened on one side with a polymer textile-reinforced mortar system. The reported damping ratios ranged from a minimum of 11 % to a maximum of 19.6 %. More recently, Padalau et al. [41] performed reverse cyclic tests on flanged brick masonry walls retrofitted on both sides using either basalt-fiber or steel welded mesh-reinforced cementitious composite systems. They reported average damping ratios ranging from 24 % to 32 %. These literature values are of the same order of magnitude as those observed at the end of the test on specimen WO2. Moreover, when compared to URM flanged walls tested by others [42], which exhibited damping ratios in the range 5–10 % for members with a flexural-rocking response, the damping factors observed herein appear to be slightly higher. Nevertheless, further research is required to validate the findings presented in this study and compare them to the response of un-strengthened members.

3.2. Two-way spanning wall

3.2.1. Load-deflection response and damage evolution

The hysteretic response and the envelope curve of wall WO3 are reported in Fig. 12. About the evolution of damage, Fig. 13 illustrates the crack pattern detected on both sides of the wall at net deflection levels of 2 mm and 4 mm, as detected by instrument HC3.

The crack pattern shown in Fig. 13 reveals the presence of pre-existing cracks (indicated by the green color) that were detected at the onset of the test along the base section of the wall, as well as on the coating surface. As discussed below, it was observed that these cracks tended to reopen during the execution of the test. It is the author's opinion that these cracks had a detrimental effect on the initial stiffness, but they did not significantly affect the maximum resistance and deflection capacity of the walls.

When loading in the outward (positive) direction, the response of the wall remained linear up to approximately + 110 kN, corresponding to a

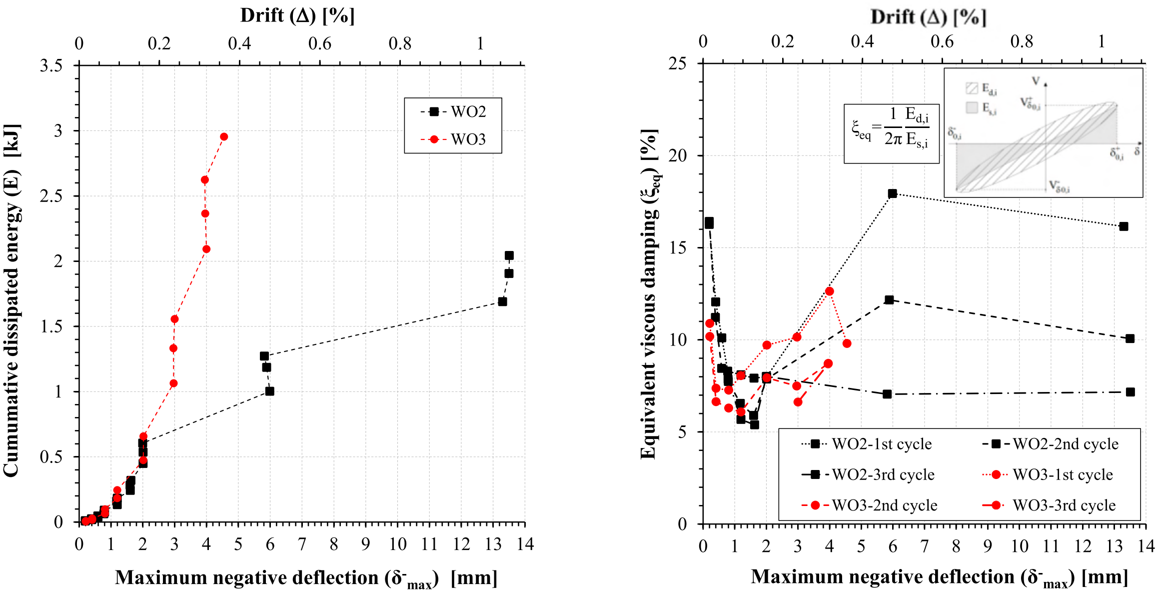

(a) (b)

Fig. 11. Results exhibited by specimens WO2 and WO3: (a) cumulative dissipated energy (a) and (b) equivalent viscous damping ratio.

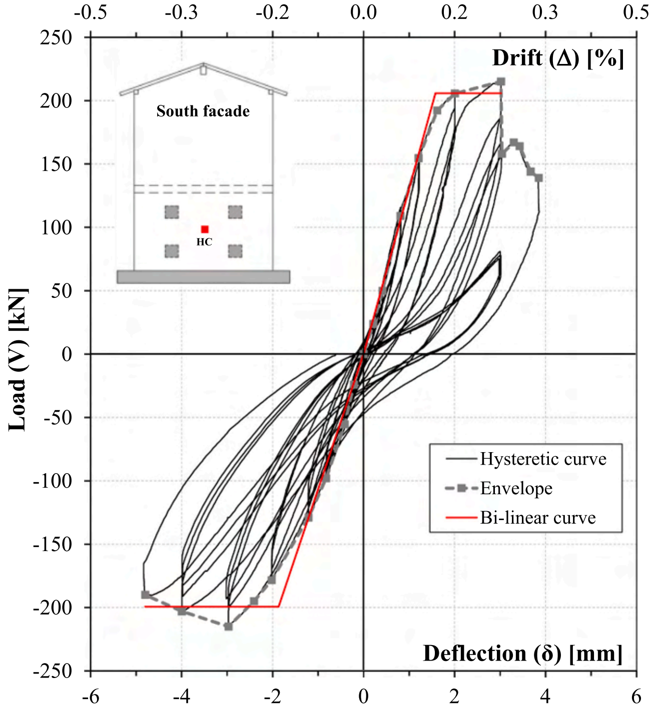

Fig. 12. Load-deflection response of the two-way spanning wall (WO3).

deflection of + 0.81 mm. At this point, vertical cracks appeared on the coating surface between the loading plates, and a horizontal crack became visible along the top side of the inner surface. As the wall was further displaced, the lateral stiffness gradually decreased due to the propagation of these cracks, which reached widths of 0.2–0.4 mm at a deflection of + 2 mm, as shown by the vertical red cracks in Fig. 13a. The wall reached its peak capacity at + 215 kN and deflection of + 3.0 mm, after which the load dropped sharply to + 158 kN. This reduction was primarily attributed to the widening of vertical cracks on the coating surface, which exceeded 1 mm in width. Simultaneously, the horizontal (red) crack at the top of the wall extended across its full width. The test was stopped at an ultimate deflection of + 3.8 mm due to localized crushing beneath one of the loading plates on the uncoated masonry surface. The final crack pattern is shown in Fig. 13b. The activation of vertical cracks (see vertical red cracks) between the loading points was expected, considering the bi-dimensional properties of the panel, which is restrained along the whole perimeter. In contrast, the development of the vertical (light blue) cracks, which bound the 1600 mm wide strip depicted in Fig. 13b, is not typical of slab elements subjected to point loads like those herein applied. However, since the horizontal resistance (Table 1) of masonry was considerably lower than the vertical one, vertical cracks formed at an early stage, preventing the wall from fully exploiting its potential resistance.

The response observed in the negative direction is very similar to that detected during positive loading. As illustrated in Fig. 12, the response remained linear up to a load of − 98 kN, corresponding to the activation of the first cracks visible on the inner surface of the wall. These cracks affected the vertical joints between the loading points, as well as the horizontal joints located in the middle of the wall. As deflection increased to − 2.0 mm, cracks further propagated across the uncoated masonry surface (see the light-blue cracks in Fig. 13a), while the green pre-existing horizontal cracks at the top and bottom of the outer face reopened, leading to further stiffness degradation. The peak load in this direction was − 215 kN at a deflection of − 3.0 mm. In the post-peak phase, sub-vertical cracks developed on the inner face, extending

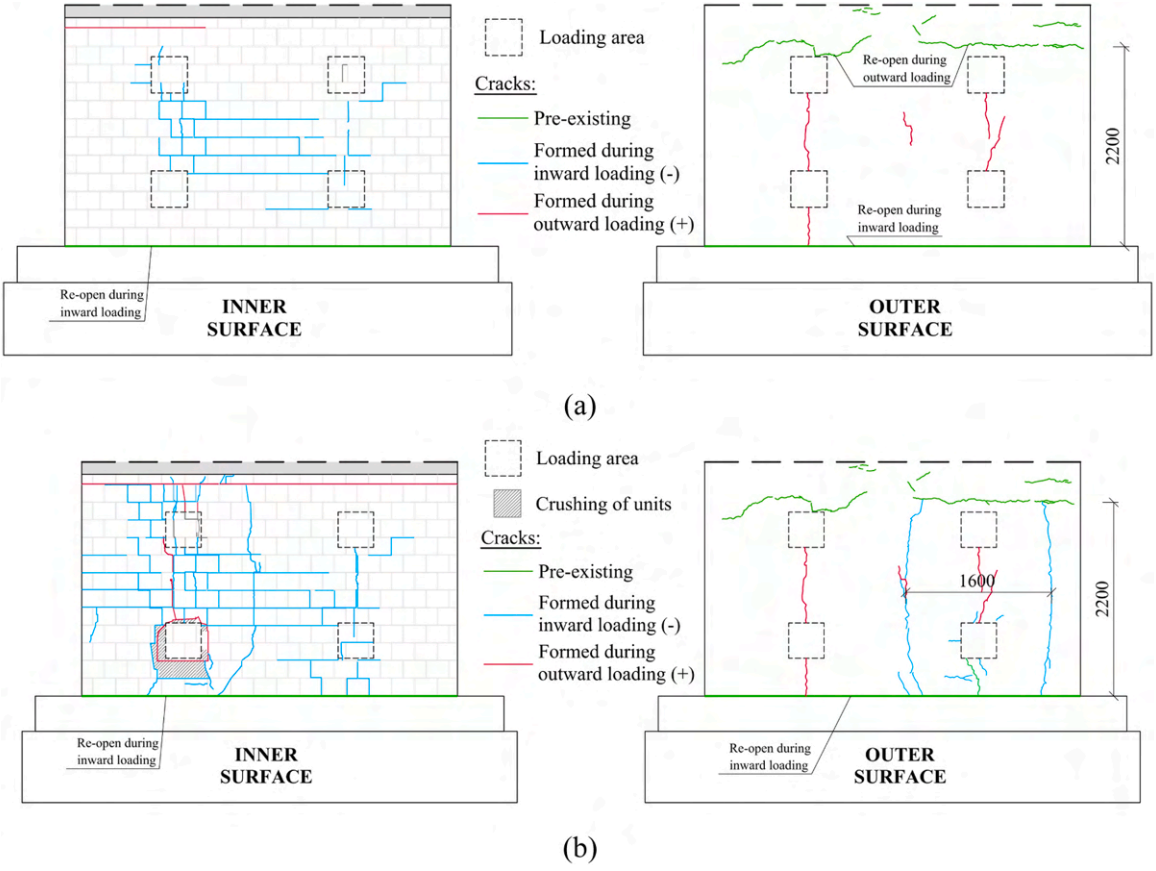

Fig. 13. Evolution of WO3 crack pattern: (a) cracks detected at δ= ±2 mm; (b) ultimate crack pattern (δ=+3.85 mm and δ=-4.8 mm). (Dimensions in [mm]).

upward from the top loading points and contributing to a gradual loss of resistance. The test was concluded at an ultimate deflection of − 4.8 mm, with the wall still resisting 88 % of its maximum resistance. At this stage, vertical cracks had extended throughout the whole thickness of the wall, as shown by the curved blue cracks in Fig. 13b.

The previous considerations suggest that the overall response of WO3 was affected by the behavior of the wall strip bounded by the vertical light-blue cracks described above (Fig. 13b), resulting in a mechanism comparable to that observed for the one-way spanning walls. The quite symmetric crack pattern in this area of the wall helps to explain why the wall reached the same maximum capacity (i.e., 215 kN) in both loading directions.

The evolution of lateral deflection over the wall height (Fig. 14), reveals that the shape remained symmetric throughout the test until severe damage occurred. The progressive damage of the wall resulted in cumulative residual displacements, which were here detected by sensors HC5, HW2 and HE2. The presence of residual displacements indicates the occurrence of a rigid OP rotation about the base section of the wall. As observed in the case of one-way spanning walls, the residual deflection at the wall supports may influence the bending resisting mechanism governing the response of the wall. Future studies will focus on analyzing the impact of support degradation on the development of this arching mechanism.

3.2.2. Initial stiffness, ultimate drift and ductility

The bi-linearization of the hysteretic curve (Fig. 12) provides

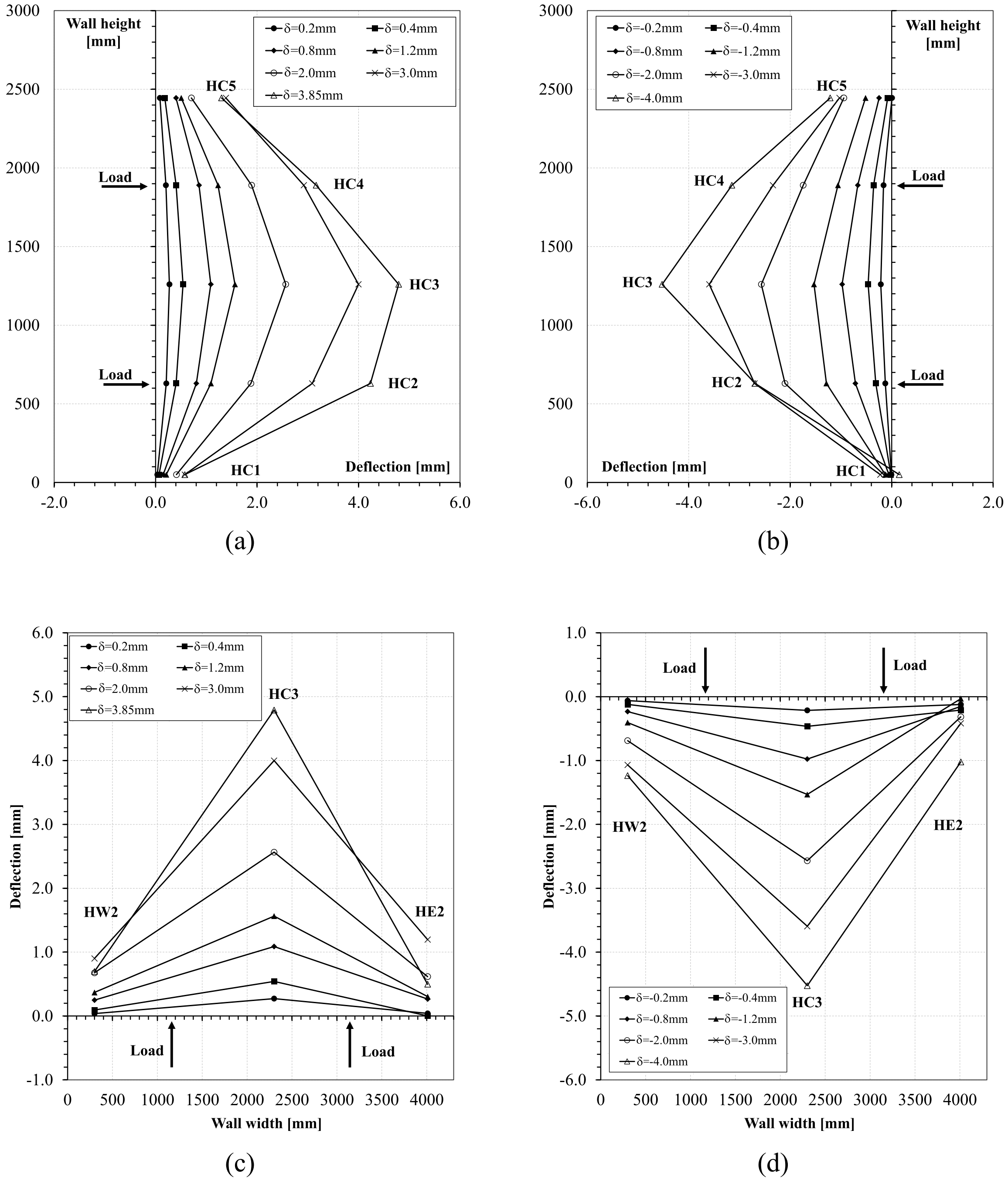

Fig. 14. Deflected profiles at different mid-span lateral deflection (δ) levels: vertical profile detected in the (a) positive and (b) negative loading direction; horizontal profile detected in the (c) positive and (d) negative loading direction.

additional information about the global behavior of the wall. The mean initial secant stiffness was equal to 119 kN/mm, as reported in Table 3. The stiffness in the positive direction (130 kN/mm) differs by 21 % as compared to that (107 kN/mm) calculated in the negative direction. The ultimate drift resulted equal to 0.24 % and 0.38 % in the positive and negative loading direction, respectively.

The ductility attained in the positive direction (μ=1.9) was 30 % lower than that (μ=2.8) observed in the negative direction. This difference in ductility is clearly due to the sudden drop of resistance that affected the response during outward loading. However, like the one-way spanning walls, both the ductility and displacement capacity in the negative direction likely took advantage from the reinforcing bars at the wall base, which helped to control the reduction in resistance during the post-peak stage.

Considering both initial stiffness and peak strength, the wall showed similar pre-peak behavior in both loading directions. Post-peak responses were also consistent, as indicated by comparable drift and ductility values in Table 3. The latter were significantly affected by the fast strength degradation following the attainment of the peak load.

3.2.3. Energy dissipation and equivalent viscous damping

The cumulative energy dissipated by wall WO3 is shown in Fig. 11a. The dissipated energy remained quite limited up to a negative lateral deflection of 1.2 mm. Between the 8th and the 9th loading cycle, corresponding respectively to a lateral deflection of about 1.2–2 mm, the dissipated energy increased with a significantly higher rate, resulting from the propagation of cracks mainly on the SFRM coating surface. During the last loading cycles the energy dissipation further increased so that the total cumulated energy attained a maximum value of 2.95 kJ, which corresponds to about 1.5 times that dissipated by the wall WO2.

As already noted in specimen WO2, the viscous damping ratio exhibited a gradual reduction as the number of cycles increased. This decrease started from an initial value of 10.8 % and reached a minimum of 6.1 % at a lateral deflection of 1.2 mm (Fig. 11b). For higher values of the deflection the damping ratio tended to increase up to a maximum of 12.6 %.

3.3. Considerations on the structural role of SFRM coating

As highlighted in the following section, the absence of a test on an un-strengthened element makes difficult to draw definitive conclusions about the actual improvements provided by the SFRM coating to the performance of URM walls. Nevertheless, the tests clearly demonstrated how the SFRM interacts with the wall and contributes to its OP response.

The first observation relates to the global response of the walls, which showed an almost symmetric OP capacity. Apparently, this result contrasts with the geometric asymmetry of the wall due to the single-sided strengthening applied. A more detailed analysis of the wall's behavior reveals that the single SFRM layer contributes to the OP capacity under both inward and outward loading. In fact, during positive (outward) loading, a primary plastic hinge developed in an intermediate region of the wall, activating the tensile capacity of the SFRM on the most stressed fiber of the cross section. When the load was reversed (inward loading), most of the outer side of the wall was in compression, except at the top and bottom sections where the outer fibers experienced tension. In these edge regions, the SFRM layer was able to provide tensile resistance due to both the continuity of the coating at the top section and the use of rebars connecting the SFRM overlay to the foundation. Therefore, regardless of the loading direction, the SFRM's tensile contribution is activated by the plastic hinges involved in the failure mechanism. This suggests also that, during outward loading, the SFRM layer can enhance the flexural strength and ductility of the top and bottom wall sections, partly due to the increased compressive strength it provides. Local reinforcement embedded within the coating in these sections, can act in conjunction with the steel fibers to further enhance flexural strength and ductility during inward loading. In practical retrofitting interventions, local reinforcing bars connecting the coating to the foundation or floor chords can be readily implemented and can be also required to enhance in-plane resistance of the walls.

When considering the global behavior of the building, the application of single-sided strengthening [23] has proven effective in increasing the in-plane resistance of the walls while also promoting the "box-behavior of the entire structure". However, when greater in-plane resistance is required, strengthening of both sides of the wall may be considered. This would also enhance the OP flexural response as well, particularly in the outward loading direction, provided that proper connection details are used to ensure continuity between the inner SFRM layer and both the top and bottom chords or foundation of the building.

4. Strengthened vs. un-strengthened walls: analytical calculation

This section provides an estimation of the potential strength increase achieved through one-sided strengthening of masonry walls. Since the tests were carried out only on strengthened walls, the expected resistance of the un-strengthened walls will be determined analytically using a resisting model accounting for one-way arching action (Fig. 15). The model assumes that the top and the bottom r.c. chords bounding the test walls are rigid enough to prevent the wall from vertical expansion and enable the development of the arch thrust. Unlike the strengthened specimens, whose bending behavior of plastic hinges can exploit the tensile contribution of SFRM coating and local reinforcement (if any), the negligible tensile resistance of masonry promotes the activation of the arching mechanism governing the ultimate resistance of the un-strengthened wall. The schematic of Fig. 15 shows two possible arch thrust mechanisms that are consistent with the external point loads (F/2). The configuration involves the activation of plastic hinges at both edge sections as well as in correspondence of either the two point loads (Type A) or only at the mid-height section (Type B). These two configurations may provide the potential limits to the OP resistance.

Based on equilibrium considerations, when the maximum arch thrust (N_a) is developed within the wall thickness (t_m), the total resistance of the wall ($V_{max,ar}$) can be calculated as follows:

$$V_{max,ar} = 2\cdot(N_a\cdot b\cdot \sin\theta) \tag{4}$$

where b is the total width of the wall and θ is the angle representing the slope of the thrust line. According to the EC6 (clause 6.3.2) [43], the bearings of the arch trust (x) at the supports and at the intermediate hinges can be both assumed as 0.1 t_m, which corresponds to a total rise of the arch equal to 0.9 t_m. Therefore, the term sinθ in the Eq. 4 results from the following relation:

$$\sin\theta = \frac{0.9\cdot t_m}{\sqrt{(h')^2 + (0.9\cdot t_m)^2}} \tag{5}$$

where h' is equal to h/4, for the configuration Type A, and h/2 for Type B. The thrust force (N_a) per unit width of the wall [43] can be estimated as follows:

$$N_a = 0.15\cdot f_{mv}\cdot t_m \tag{6}$$

where f_{mv} is the compressive strength of masonry in the direction of the arch thrust, which is equal to the compressive strength parallel to holes reported in Table 1. The adopted one-way arching model does not consider several mechanisms that may either reduce (e.g., pre-existing damage in the masonry, second-order effects, arch deflection under lateral loads, deformability of the concrete chords, relative sliding between the wall and the chords, or local shear failure/crushing of units at the edges) or enhance (e.g., bi-axial bending in the case of two-way spanning walls) the overall OP resistance of the wall. Many of these effects are particularly challenging to assess accurately, especially in the

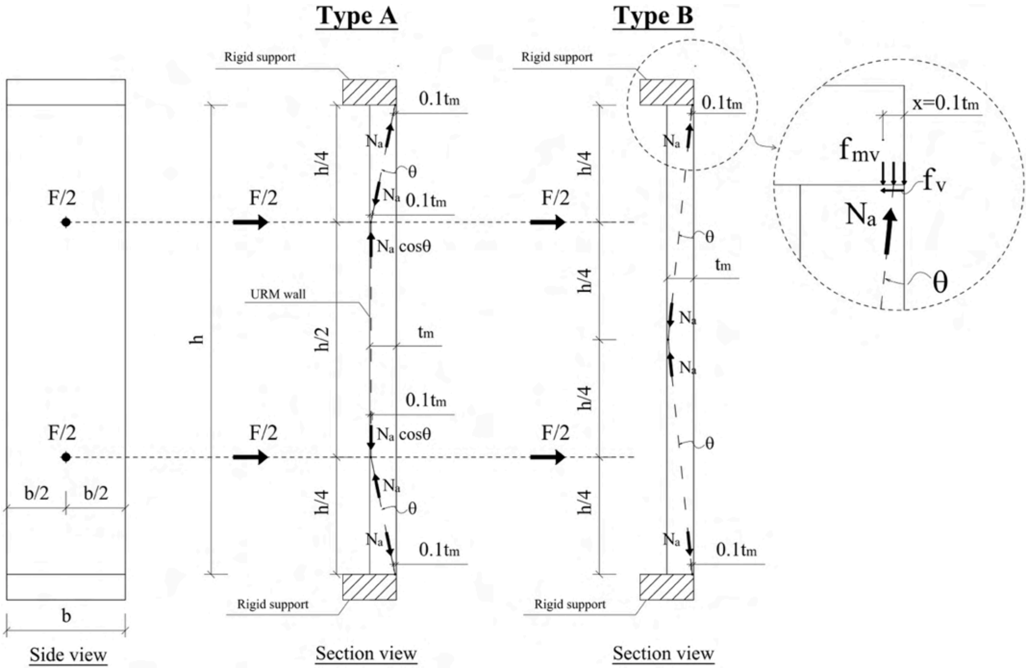

Fig. 15. Schematic of the adopted arch resisting mechanisms.

absence of experimental data. About local failure of units, the formulations reported by the NTC18 [37] and the EC6 [43] can be used to impose an upper limit on the maximum strength of the masonry panel due to shear or crushing failure of the masonry units [44]. That is, the maximum lateral shear strength (V_{lim}), which represents the upper limit to the total resistance ($V_{max,ar}$), can be estimated as follows:

$$V_{lim} = 2\cdot(x\cdot b\cdot f_v) = 2\cdot(0.1\cdot t_m\cdot b\cdot f_v) \tag{7}$$

where f_v is the shear strength of masonry resulting from the following relation:

$$f_v = f_{v0} + \mu\cdot f_{mv} \quad \leq \quad 0.065\cdot f_b \tag{8}$$

where f_{v0} and μ are the mean direct shear resistance under zero normal stress and the friction angle of mortar joints, respectively; f_b= 12.7 MPa is the mean compressive strength of units parallel to the holes (Table 1). The characteristic strength $f_{v0,k}$ was assumed equal to 0.2 MPa, as recommended by the EC6 (clause 3.6.2), whereas the corresponding mean value was calculated as $f_{v0}=f_{v0,k}/0.8 = 0.25$ MPa. The friction angle (μ) was assumed to be equal to 0.577 (i.e., friction angle of 30°). The maximum allowable resistance ($V_{max,an}$) corresponds to the weakest of the previous mechanisms, i.e.

$$V_{max,an} = \min\left(V_{max,ar}\ ;\ V_{lim}\right) \tag{9}$$

Note that the adopted one-way arching mechanism considers the activation of a failure pattern symmetric as compared to the loads and to boundaries. This condition could not be totally representative of the test, as the specimen could exhibit the activation of a single intermediate plastic hinge.

Table 4 presents a summary of the input data used in the model, along with the main results of the calculations. The term $V_{max,exp}$ corresponds to the maximum experimental capacity of the wall (see also Table 3) obtained by averaging the values attained in the positive and in the negative direction. The last column of the table compares the experimental resistance with the corresponding analytical prediction ($V_{max,an}$).

By considering the one-way spanning walls (i.e. WO1 and WO2), the experimental resistance was found to be 123 % and 200 % higher respectively than the capacity of the URM walls estimated according to the mechanism Type A and B.

The capacity of the wall WO3 is calculated by the same one-way scheme (Fig. 15) adopted for the walls WO1 and WO2. This assumption was consistent with the failure mechanism developed by the test walls (Fig. 13) as well as by the deflected profiles (Fig. 14), which highlighted the activation of plastic hinges in areas near the point loads. The lack of significant cracks extending from the point loads to the vertical left and right sides of the panel suggests that the wall was unable to develop resisting mechanisms typical of slabs supported on all four sides. Hence, the maximum OP capacity of the un-strengthened wall was computed based on the total resistance of a one-way spanning wall having a total width of b= 2 × 1600 mm= 3200 mm, corresponding to twice the width of the wall strip bounded by the vertical light-blue cracks shown in Fig. 13b. As reported in Table 4, the expected

Table 4
Flexural capacity of test walls: comparison of experimental results and analytical predictions.

Specimen	h	t	b	sinθ	N_a	$V_{max,ar}$	V_{lim}	$V_{max,an}$	$V_{max,exp}$	$\frac{V_{max,exp}}{V_{max,an}}$
	[mm]	[mm]	[mm]	[-]	[N/mm]	[kN]	[kN]	[kN]	[kN]	[-]
WO1	2520	200	1000	0.275 (A) 0.141 (B)	87	47.9 (A) 24.5 (B)	33.0	33.0 (A) 24.5 (B)	73.5	2.2 (A) 3.0 (B)
WO2	2520	200	1000	0.275 (A) 0.141 (B)	87	47.9 (A) 24.5 (B)	33.0	33.0 (A) 24.5 (B)	73.1	2.2 (A) 3.0 (B)
WO3	2520	200	3200	0.275 (A) 0.141 (B)	87	153.3 (A) 78.4 (B)	105.6	105.6 (A) 78.4 (B)	215.0	2.0 (A) 2.7 (B)

Note: (A) refers to the configuration Type A; (B) refers to the configuration Type B.

increment of capacity for WO3, referred to the mechanisms Type A and B, are equal to 104 % and 174 %, which are aligned with the predicted capacity enhancements for WO1 and WO2. The local shear-crushing failure of clay blocks was the mechanism governing the maximum lateral resistance of all the specimens.

It is worth remarking that the comparison presented in this section provides only an estimate of the potential strength increase achievable through retrofitting with SFRM coating, as the analytical model cannot consider most of the detrimental or beneficial mechanisms described above.

5. Concluding remarks

The results of in-situ OP bending monotonic and reverse cyclic tests carried out on three walls strengthened on one side with SFRM coating were presented. The test program included two one-way and one two-way spanning walls. The loading setup was specifically designed to investigate the walls' OP bending behavior while neglecting the interaction with in-plane actions typically occurring during real seismic events. All tested specimens were part of a full-scale building examined in earlier research.

Based on the discussion reported in the paper, the following main conclusions can be stated:

- The use of SFRM with a significant post-cracking resistance and ductility promoted the internal stress redistribution well highlighted by multiple vertical and horizontal cracks spread mainly on the uncoated surface of masonry.
- The OP drift capacity attained by the one-way spanning walls was approximately equal to 0.86 %, on average. On the contrary, the drift capacity of the two-way spanning wall was about 0.35 %. It should be underlined that, after attaining the maximum capacity, the SFRM was not always able to control the post-peak response of the wall, leading to a gradual decrease of resistance.
- As the lateral deflection of the specimens increased, the equivalent viscous damping generally decreased before stabilizing within a relatively narrow range (6–10 %), corresponding to lateral drifts between 0.05 % and 0.2 %. At the end of the tests, specimens WO2 and WO3 exhibited maximum damping ratios of 18 % and 12.6 %, respectively.
- Based on the classical arch resisting mechanism included in the EC6, a prediction of the maximum capacity of the un-strengthened walls was carried out. The comparison of the experimental strengths with the predicted ones provided an estimate of the potential capacity enhancement obtained after retrofitting the wall with SFRM coating. The results showed that the expected increment in capacity ranged from the minimum of 104 %-174 %, for the two-way spanning wall, to a maximum of 123 %-200 % for the one-way spanning specimens. The results of this research represent an important contribution to the state of knowledge as they confirm the potential ability of SFRM coating to improve the flexural resistance of masonry members.
- The proposed analytical model provides an estimation of the OP capacity of the walls. The calculations indicated that single-sided strengthening can enhance resistance in both outward and inward directions, provided that the reinforcement layer is continuous over the whole height of the wall. In cases where discontinuities occur along the horizontal cross-section of the coating, the adoption of short conventional rebars locally placed to bridge the discontinuity proved to be effective in transferring the tensile stresses over the coating section. However, it is important to note that these conclusions are entirely based on predictions from the analytical model, which relies on simplified assumptions regarding the failure mechanism and boundary conditions.

The conclusions presented herein should not be generalized to all existing masonry typologies and SFRM properties.

The test results discussed above along with the analytical predictions demonstrated the potential enhancement in the OP behavior of masonry walls achievable by single layer of SFRM on the external surface of the wall.

Further experimental and numerical studies are needed to extend the results to the double-sided strengthened walls. In this regard, a numerical parametric study, although not included here as it falls outside the scope of this work, would help to extend and generalize the results reported above.

CRediT authorship contribution statement

Fausto Minelli: Writing – review & editing, Project administration, Methodology. **Giovanni Plizzari:** Writing – review & editing, Project administration, Funding acquisition. **Luca Facconi:** Writing – original draft, Supervision, Project administration, Methodology, Investigation, Conceptualization. **Sara S. Lucchini:** Supervision, Investigation, Data curation.

Declaration of Competing Interest

The authors declare that they have no known competing financial interests or personal relationships that could have appeared to influence the work reported in this paper.

Acknowledgements

The research work is part of the Health&Wealth project "Sismacomf" supported by the University of Brescia and by Tecnologia e Ricerca Italiana S.r.l. (TRI S.r.l), which are gratefully acknowledged. Special thanks go to Engs Debora Pagnoni and Matteo Bergoli for their contribution to the tests' execution and data post-processing. The financial support provided by the ReLUIS-DPC project 2019–2021 is also gratefully acknowledged.

Data availability

Data will be made available on request.

References

[1] Tomazevic M. Earthquake-resistant Design of Masonry Buildings. World Scientific Publishing Co. Pte. Ltd.; 1999. ISBN 1-86094-066-8.

[2] Angel R, Abrams DP, Shapiro D, Uzarski J, Webster M. Behavior of reinforced concrete frames with masonry infills. Civ Eng Stud 1994. SRS-589.

[3] Drysdale RG, Essawy AS. Out-of-plane bending of concrete block walls. J Struct Eng 1988;114(1):121–33.

[4] Valluzzi MR, Da Porto F, Garbin E, Panizza M. Out-of-plane behaviour of infill masonry panels strengthened with composite materials. Mater Struct 2014;47:2131–45.

[5] Jafari S, Rots JG, Esposito R, Messali F. Characterizing the material properties of Dutch unreinforced masonry. Procedia Eng 2017;193:250–7.

[6] Costa AA, Arède A, Costa A, Oliveira CS. Out-of-plane behaviour of existing stone masonry buildings: experimental evaluation. Bull Earthq Eng 2012;10:93–111.

[7] Derakhshan H, Dizhur D, Griffith MC, Ingham JM. In situ out-of-plane testing of as-built and retrofitted unreinforced masonry walls. J Struct Eng 2014;140(6):04014022.

[8] Derakhshan H, Lucas W, Visintin P, Griffith MC. Out-of-plane Strength of Existing Two-way Spanning Solid and Cavity Unreinforced Masonry Walls. In: Structures. Elsevier; 2018. p. 88–101. 13.

[9] Calvi GM, Kingsley GR, Magenes G. Testing of masonry structures for seismic assessment. Earthq Spectra 1996;12(1):145–62.

[10] Applied Technology Council (ATC). NEHRP commentary on the guidelines for the seismic rehabilitation of buildings. FEMA Publication 274. Washington, D. C.: Building Seismic Safety Council; 1997.

[11] D'Ambra C, Lignola GP, Prota A, Sacco E, Fabbrocino F. Experimental performance of FRCM retrofit on out-of-plane behaviour of clay brick walls. Composites Part B Engineering 2018;148:198–206.

[12] De Santis S, De Canio G, de Felice G, Meriggi P, Roselli I. Out-of-plane seismic retrofitting of masonry walls with textile reinforced mortar composites. Bull Earthq Eng 2019;17(11):6265–300.

[13] D`antino T, Carozzi FG, Colombi P, Poggi C. Out-of-plane maximum resisting bending moment of masonry walls strengthened with FRCM composites. Compos Struct 2018;202:881–96.

[14] Papanicolaou C, Triantafillou T, Lekka M. Externally bonded grids as strengthening and seismic retrofitting materials of masonry panels. Constr Build Mater 2011;25 (2):504–14.

[15] Willis CR, Seracino R, Griffith MC. Out-of-plane strength of brick masonry retrofitted with horizontal NSM CFRP strips. Eng Struct 2010;32(2):547–55.

[16] Hamed E, Rabinovitch O. Lateral out-of-plane strengthening of masonry walls with composite materials. J Compos Constr 2010;14(4):376–87.

[17] Gattesco N, Boem I. Out-of-plane behavior of reinforced masonry walls: experimental and numerical study. Composites part B engineering 2017;128: 39–52.

[18] Monaco A, Minafò G, Cucchiara C, D'Anna J, La Mendola L. Finite element analysis of the out-of-plane behavior of FRP strengthened masonry panels. Composites Part B Engineering 2017;115:188–202.

[19] Sevil T, Baran M, Bilir T, Canbay E. Use of steel fiber reinforced mortar for seismic strengthening. Constr Build Mater 2011;25(2):892–9.

[20] Bustos-García A, Moreno-Fernández E, Zavalis R, Valivonis J. Diagonal compression tests on masonry wallets coated with mortars reinforced with glass fibers. Mater Struct 2019;52:1–13.

[21] Simoncello N, Zampieri P, Gonzalez-Libreros J, Pellegrino C. Experimental behaviour of damaged masonry arches strengthened with steel fiber reinforced mortar (SFRM). Composites Part B Engineering 2019;177:107386.

[22] Del Zoppo M, Di Ludovico M, Balsamo A, Prota A. Fibre reinforced mortars for the out-of-plane strengthening of masonry walls. Procedia Struct Integr 2023;44: 2158–65.

[23] Lucchini SS, Facconi L, Minelli F, Plizzari G. Cyclic test on a full-scale unreinforced masonry building repaired with steel fiber-reinforced mortar coating. J Struct Eng 2021;147(6):04021059.

[24] Lucchini SS, Facconi L, Minelli F, Plizzari G. Retrofitting unreinforced masonry by steel fiber reinforced mortar coating: uniaxial and diagonal compression tests. Mater Struct 2020;53(6):144.

[25] EN 1015-11:2019. Methods of Test for Mortar for Masonry - Part 11: Determination of Flexural and Compressive Strength of Hardened Mortar.

[26] EN 12390-13. Testing hardened concrete - Part 13: Determination of Secant Modulus of Elasticity in Compression." (in Italian).

[27] EN 14651:2005+A1:2007. Test method for Metallic Fibre Concrete - Measuring the Flexural Tensile Strength (Limit of Proportionality (LOP), residual).

[28] EN 1992-1-1:2023. Eurocode 2 – Design of Concrete Structures. Part 1-1: General rules, and rules for buildings, bridges and civil engineering structures.

[29] EN 772-1: 2015. Methods of test for masonry units—Part 1: Determination of compressive strength. EN 772-1. Brussels, Belgium: CEN.

[30] EN 1052-1: 1998. Methods of test for masonry - Part 1: Determination of Compressive Strength.

[31] ASTM E519-02 (2002). Standard Test Method for Diagonal Tension (Shear) in Masonry Assemblages. West Conshohocken, PA.

[32] Hamoush SA, McGinley MW, Mlakar P, Scott D, Murray K. Out-of-plane strengthening of masonry walls with reinforced composites. J Compos Constr 2001; 5(3):139–45.

[33] Lin Y, Lawley D, Wotherspoon L, Ingham JM. Out-of-plane Testing of Unreinforced Masonry Walls Strengthened Using ECC Shotcrete, In: Structures. Elsevier; 2016. p. 33–42. 7.

[34] Walsh K, Dizhur D, Giongo I, Derakhshan H, Ingham J. Predicted Versus Experimental Out-of-plane Force-displacement Behaviour of Unreinforced Masonry Walls. In: Structures. Elsevier; 2018. p. 292–306. 15.

[35] Derakhshan H, Lucas W, Visintin P, Griffith MC. Out-of-plane Strength of Existing Two-way Spanning Solid and Cavity Unreinforced Masonry Walls. In: Structures. Elsevier; 2018. p. 88–101. 13.

[36] Kabir H, Wu J, Dahal S, Joo T, Garg N. Automated estimation of cementitious sorptivity via computer vision. Nat Commun 2024;15(1):9935.

[37] NTC (Norme Tecniche per le Costruzioni). Decreto ministeriale del 17/01/ 18–Aggiornamento delle norme tecniche per le costruzioni, 17 gennaio 2018 ([In Italian.]). Rome: Ministero delle Infrastrutture; 2018.

[38] Chopra AK. Dynamics of structures: theory and applications to earthquake engineering. Hoboken: Prentice Hall; 1995. https://doi.org/10.1002/eqe.4290240809.

[39] Gams M, Boem I, Gattesco N, Rizzi E, Dudine A. Experimental study on the seismic enhancement of brick masonry spandrels using a single-sided composite reinforced mortar coating. Bull Earthq Eng 2024;22(5):2531–52.

[40] Ismail N, Ingham JM. In-plane and out-of-plane testing of unreinforced masonry walls strengthened using polymer textile reinforced mortar. Eng Struct 2016;118: 167–77.

[41] Padalu PKVR, Singh Y, Das S. Cyclic two-way out-of-plane testing of unreinforced masonry walls retrofitted using composite materials. Constr Build Mater 2020;238: 117784.

[42] Kallioras S, Graziotti F. Experimental insights into the seismic behaviour of flanged URM walls. Eng Struct 2025;322:119057.

[43] EN 1996-1-1:2005. Eurocode 6: Design of Masonry Structures - Part 1-1: General rules for reinforced and unreinforced masonry structures.

[44] Milanesi RR, Morandi P, Hak S, Magenes G. Experiment-based out-of-plane resistance of strong masonry infills for codified applications. Eng Struct 2021;242: 112525.